The Astrophysical Journal, 893:133 (8pp), 2020 April 20 https://doi.org/10.3847/1538-4357/ab7f2c

On Stellar Evolution in a Neutrino Hertzsprung–Russell Diagram

Ebraheem Farag[1], F. X. Timmes[1,2], Morgan Taylor[1], Kelly M. Patton[3], and R. Farmer[4]
[1] School of Earth and Space Exploration, Arizona State University, Tempe, AZ 85287, USA; ekfarag@asu.edu
[2] Joint Institute for Nuclear Astrophysics—Center for the Evolution of the Elements, USA
[3] Department of Physics and Astronomy, Colby College, Waterville, ME 04961, USA
[4] Anton Pannenkoek Institute for Astronomy and GRAPPA, University of Amsterdam, NL-1090 GE Amsterdam, The Netherlands
Received 2019 November 26; revised 2020 March 4; accepted 2020 March 10; published 2020 April 23

Abstract

We explore the evolution of a select grid of solar metallicity stellar models from their pre-main-sequence phase to near their final fates in a neutrino Hertzsprung–Russell diagram, where the neutrino luminosity replaces the traditional photon luminosity. Using a calibrated MESA solar model for the solar neutrino luminosity ($L_{\nu,\odot} = 0.02398 \cdot L_{\gamma,\odot} = 9.1795 \times 10^{31}$ erg s^{-1}) as a normalization, we identify ≃0.3 MeV electron neutrino emission from helium burning during the helium flash (peak $L_\nu/L_{\nu,\odot} \simeq 10^4$, flux $\Phi_{\nu,\mathrm{He\ flash}} \simeq 170\ (10\ \mathrm{pc}/d)^2$ cm^{-2} s^{-1} for a star located at a distance of d parsec, timescale ≃3 days) and the thermal pulse (peak $L_\nu/L_{\nu,\odot} \simeq 10^9$, flux $\Phi_{\nu,\mathrm{TP}} \simeq 1.7 \times 10^7\ (10\ \mathrm{pc}/d)^2$ cm^{-2} s^{-1}, timescale ≃0.1 yr) phases of evolution in low-mass stars as potential probes for stellar neutrino astronomy. We also delineate the contribution of neutrinos from nuclear reactions and thermal processes to the total neutrino loss along the stellar tracks in a neutrino Hertzsprung–Russell diagram. We find, broadly but with exceptions, that neutrinos from nuclear reactions dominate whenever hydrogen and helium burn, and that neutrinos from thermal processes dominate otherwise.

Unified Astronomy Thesaurus concepts: Stellar physics (1621); Stellar evolution (1599); Stellar evolutionary tracks (1600); Hertzsprung Russell diagram (725); Neutrino astronomy (1100)

1. Introduction

Stars radiate energy by releasing photons from the stellar surface and neutrinos from the stellar interior. In the interior, weak reactions produce electron neutrinos by thermal processes, electron and positron captures on nuclei, and nuclear decays. Neutrinos interact feebly with baryonic matter, with typical cross sections of ≃10^{-44} cm^2 as opposed to typical photon cross sections of ≃10^{-24} cm^2, escaping from the star unhindered in circumstances where photons are trapped.

Neutrino losses play key roles on the main sequence in the case of the Sun (Bahcall & Pinsonneault 1992; Bahcall et al. 2005; Haxton et al. 2013), during the helium flash in red giants (Ramadurai 1976; Sweigart & Gross 1978; Raffelt & Weiss 1992; Catelan et al. 1996), in the conversion of ^{14}N to ^{22}Ne during core helium burning (Serenelli & Fukugita 2005), for the cooling of white dwarfs (WDs; van Horn 1971; Kawaler et al. 1986; Fontaine et al. 2001; Althaus et al. 2010; Bischoff-Kim & Montgomery 2018), during core carbon burning (Ramadurai 1984; Aufderheide 1993; Meakin & Arnett 2007; Cristini et al. 2017, 2019), for pre-supernova stars (Odrzywolek 2009; Kutschera et al. 2009; Patton et al. 2017a, 2017b), for both core-collapse supernovae (e.g., Janka 2017) and electron-capture supernovae (Ray et al. 1984; Jones et al. 2013), for the cooling of neutron stars (Nomoto & Tsuruta 1981; Potekhin et al. 2015), during X-ray bursts, (Fujimoto et al. 1987; Goodwin et al. 2019), for accretion disks around black holes (Birkl et al. 2007; Fryer et al. 2014; Uribe Suárez & Rueda Hernandez 2019) during neutron star mergers (Albert et al. 2017; Kyutoku & Kashiyama 2018), and for nucleosynthesis from the ν-process (Woosley et al. 1990), νp process (McLaughlin & Fuller 1995; Fröhlich et al. 2006), and r-process (e.g., Kajino et al. 2019).

Neutrino production from thermal processes mainly depends on the ambient thermodynamic conditions (Fowler & Hoyle 1964; Beaudet et al. 1967; Schinder et al. 1987; Itoh et al. 1996a). Neutrino production from electron/positron captures and nuclear decays have a stronger dependence on the isotopic composition (Fuller et al. 1980, 1982a, 1982b, 1985; Langanke & Martínez-Pinedo 2000, 2014; Misch et al. 2018), and thus on the network of nuclear reactions that take place in the stellar interior. These two classes of neutrino production thus carry complementary information about the interior of stars (Patton et al. 2017a, 2017b).

Neutrino astronomy has been limited, so far, to the Sun (Borexino Collaboration et al. 2018), supernova 1987A (Alekseev et al. 1987; Bionta et al. 1987; Hirata et al. 1987, 1988), and the blazar TXS 0506+056 (IceCube Collaboration et al. 2018a, 2018b). However, the Super-Kamiokande with Gadolinium (Simpson et al. 2019), Jiangmen Underground Neutrino Observatory (Li 2014; Brugière 2017), and XENON (Newstead et al. 2019) experiments usher in a new generation of multi-purpose neutrino detectors designed to open new avenues for potentially observing currently undetected neutrinos.

This article is novel in exploring the evolution of stellar models in a neutrino Hertzsprung–Russell (H-R) diagram, where the traditional photon luminosity is replaced with the neutrino luminosity. This exploration provides targets for current, forthcoming, and future generations of neutrino detectors as well as providing estimates of the stellar neutrino background signal. In Section 2 we describe the input physics and solar normalization of the stellar models. In Section 3 we present our main results, and in Section 4 we discuss and summarize our results.

2. Stellar Models

2.1. Input Physics

We model the evolution of stars with initial masses $M = 1$, 2, 3, 15, 25, 30, 35, and 40 $M_\odot$ from the pre-main sequence (PMS) to a WD for the lower masses, or the onset of core collapse for the higher masses. These masses are chosen to delineate features in a forthcoming neutrino H-R diagram. We use MESA revision r12115 to construct our stellar models (Paxton et al. 2011, 2013, 2015, 2018, 2019). Each star is modeled as a single, non-rotating, mass losing, solar metallicity object. The files to reproduce our work are publicly available at doi:10.5281/zenodo.3634068.

We use the built-in MESA nuclear reaction network mesa_49 for low-mass stars and mesa_204 for high-mass stars. Relatively large nuclear networks are required to fully capture the energy generation rate, and thus the neutrino luminosity from β-processes, in neutron-rich compositions. The current defaults for nuclear reaction rates are described in Appendix A.2 of Paxton et al. (2019). Rates are taken from a combination of NACRE (Angulo et al. 1999) and the Joint Institute for Nuclear Astrophysics REACLIB library (default version, dated 2017 October 20; Cyburt et al. 2010). The MESA screening corrections are from Chugunov et al. (2007), which includes a physical parameterization for the intermediate screening regime and reduces to the familiar weak (Dewitt et al. 1973; Graboske et al. 1973) and strong (Alastuey & Jancovici 1978; Itoh et al. 1979) limits at small and large values of the plasma coupling parameter. All the weak reaction rates are based (in order of precedence) on the tabulations of Langanke & Martínez-Pinedo (2000), Oda et al. (1994), and Fuller et al. (1985).

The three most dominant thermal neutrino processes are plasmon decay ($\gamma_{\rm plasmon} \rightarrow \nu_e + \bar{\nu}_e$), photoneutrino production ($e^- + \gamma \rightarrow e^- + \nu_e + \bar{\nu}_e$), and pair annihilation ($e^- + e^+ \rightarrow \nu_e + \bar{\nu}_e$). The bremsstrahlung ($e^- + {}^{A}{\rm Z} \rightarrow e^- + {}^{A}{\rm Z} + \nu_e + \bar{\nu}_e$) and recombination ($e^-_{\rm continuum} \rightarrow e^-_{\rm bound} + \nu_e + \bar{\nu}_e$) channels play smaller roles. The total emissivities of all these processes, over a range of temperatures and densities, are discussed in Itoh et al. (1989, 1992, 1996a, 1996b) and implemented in the MESA thermal neutrino loss module. Differential rates and emissivities of selected thermal neutrino processes are discussed in Ratković et al. (2003), Dutta et al. (2004), Misiaszek et al. (2006), Odrzywołek (2007), Kato et al. (2015), and Patton et al. (2017a, 2017b).

The models approximate convection using the recipes described in Paxton et al. (2019, 2018). The adopted values of the mixing-length parameter α, and overshooting parameter $f_{\rm ov}$, as well as the initial hydrogen fraction X, helium fraction Y, and metallicity Z are determined from our calibrated solar model.

2.2. Solar Neutrino Luminosity Normalization

We perform a solar model calibration to reproduce the present day neutrino flux (Villante et al. 2014). We iterate on differences between the final model at $t_\odot = 4.568$ Gyr (Bouvier & Wadhwa 2010) and the solar radius, $R_\odot = 6.9566 \times 10^{10}$ cm, solar luminosity, $L_{\gamma,\odot} = 3.828 \times 10^{33}$ erg s^{-1} (Prša et al. 2016), and surface heavy element abundance Z/X. We use the built-in MESA simplex module to iteratively vary the mixing-length parameter, α, and the initial composition X, Y, and Z, including the effects of element diffusion (Thoul et al. 1994; Paxton et al. 2018). This calibration is performed for two estimates of; the heavy element abundance at the surface of the Sun, $Z/X = 0.0181$ (Asplund et al. 2009) and $Z/X = 0.0229$ (Grevesse & Sauval 1998). We adopt a small amount of exponential convective overshooting (Herwig 2000) by choosing $f_{\rm ov} = 0.016$ as used in the Mesa Isochrones and Stellar Tracks (MIST) isochrones (Choi et al. 2016). Separate implementations of convective overshooting at the base of the solar convection zone can be found in Christensen-Dalsgaard et al. (2011) and Zhang et al. (2019). Our calibrated solar models do not include the structural effects of rotational deformation or the effects of rotational mixing. Calibrated parameters are listed in Table 1. We use the abbreviations AGSS09 = Asplund et al. (2009) photospheric abundances mixture, and GS98 = Grevesse & Sauval (1998) meteoric abundance mixture in all Tables. The AGSS09 solar model is calculated using OPAL opacities (Iglesias & Rogers 1996), and the GS98 solar model is calculated using the Opacity Project opacities (Badnell et al. 2005). See Vinyoles et al. (2017) for updated approaches toward standard solar models.

Table 1
Solar Calibration Parameters

Component	AGSS09	GS98
$X_{\rm o}$	0.7200	0.7108
$Y_{\rm o}$	0.2654	0.2710
$\alpha_{\rm mlt}$	2.120	2.155
$(Z/X)_{\rm surf}$	0.0181	0.0229
$L_{\nu,\odot}/L_{\gamma,\odot}$	0.02398	0.02422

Figure 1 shows the fractional difference in sound speed, δc, and density, $\delta\rho$, between our calibrated solar models and the inferred helioseismic values, see Basu et al. (2009). Calculated values for helioseimic quantities are shown in Table 2. Disagreements arise from differences in the solar abundance profiles, equation of state, opacities, model atmospheres, treatment of convection, and the absence of rotational mixing. The task of correcting these disagreements is the subject of ongoing research, see Bergemann & Serenelli (2014) and Serenelli (2016). Nonetheless, our seismic results appear similar to those in Villante et al. (2014) and Asplund et al. (2009).

Neutrinos are produced during H-burning on the main sequence from the proton–proton (pp) chain reactions p(p,e^+ ν_e)^{2}H, p(e^-p,ν_e)^{2}H, ^{3}He(p,e^+ ν_e)^{4}He, ^{7}Be(e^-,ν_e)^{7}Li, ^{8}B(,e^+ ν_e)^{8}Be, and the CNO cycle reactions ^{13}N(,e^+ ν_e)^{13}C, ^{13}N(e^-,ν_e)^{13}C, ^{15}O(,e^+ ν_e)^{15}N, ^{15}O(e^-,ν_e)^{15}N, ^{17}F(,e^+ ν_e)^{17}O, ^{17}F(e^-,ν_e)^{17}O, ^{18}F(,e^+ ν_e)^{18}O, where electron-capture reactions on CNO nuclei are included (Stonehill et al. 2004). Higher temperatures can trigger the production of nuclear reaction neutrinos from the H-burning hot CNO, Ne–Na, and Mg–Al cycles.

The neutrino flux in the solar interior is strongly dependent on the core temperature (see Bahcall & Ulmer 1996). Standard solar models that accurately predict temperatures near the solar core should also generate comparable neutrino fluxes to solar neutrino data. Neutrino fluxes are calculated from each solar model and compared to observations in Table 3. Our predicted neutrino fluxes are similar to Villante et al. (2014) and Haxton et al. (2013). We adopt the AGSS09 MESA model, calculated using OPAL opacities, as the standard in this article. Specifically, we use $L_{\nu,\odot} = 0.02398 \cdot L_{\gamma,\odot} = 9.1795 \times 10^{31}$ erg s^{-1} as the normalization for the neutrino H-R diagram.

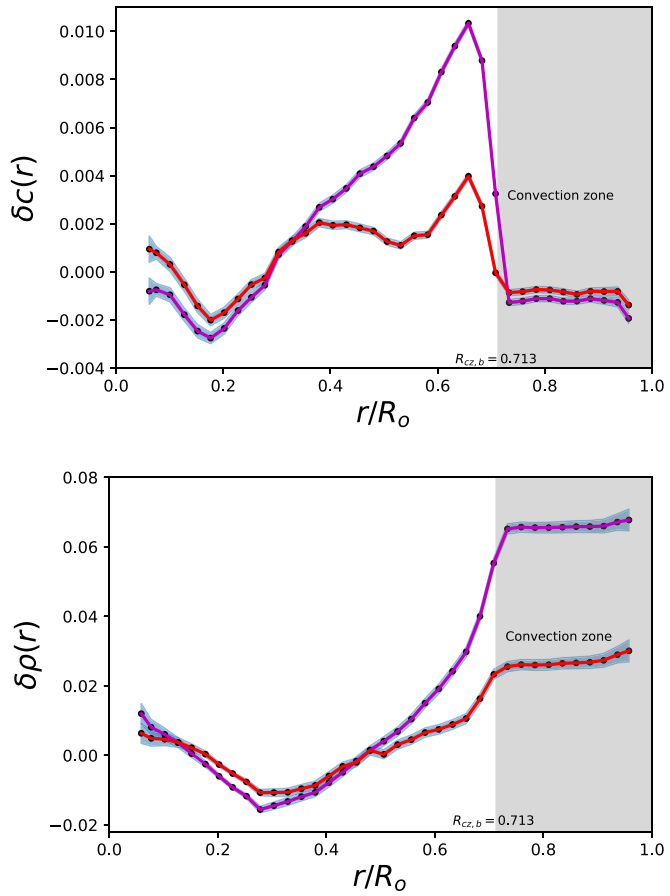

Figure 1. Fractional sound speed and density differences, $\delta c = (c_{\rm obs} - c(r))/c(r)$ and $\delta\rho = (\rho_{\rm obs} - \rho(r))/\rho(r)$, between the values predicted by the calibrated MESA standard solar model, $c(r)$ and $\rho(r)$, and the values inferred from helioseismic data (Basu et al. 2009), $c_{\rm obs}$ and $\rho_{\rm obs}$. Black dots mark locations where δc and $\delta\rho$ are evaluated. Purple curves are for AGSS09 and red curves are for GS98. The gray band shows the convective region, with the radius at the base of the convection zone $R_{\rm cz,b}$ marked. The 3σ uncertainties are shown as the blue bands.

Table 2
Properties of the Solar-calibrated Model

Component	AGSS09	GS98	Observed[a]
$R_{\rm cz,b}/R_\odot$	0.7256	0.7178	0.713 ± 0.001
$Y_{\rm surf}$	0.2396	0.2460	0.2485 ± 0.0035

Note.
[a] The helioseismic derived radius at the bottom of the convective zone, $R_{\rm cz,b}$, and surface He mass fraction, $Y_{\rm surf}$, are from Basu & Antia (1997) and Basu & Antia (2004).

3. Evolution in a Neutrino H-R Diagram

Stars are powered mainly by fusion reactions throughout their life, but weak reactions play a key role in determining their structure, energy budget, and nucleosynthesis. A fundamental aspect of weak reactions for stellar evolution is that they facilitate hydrogen fusion into helium (for universes and stellar evolution without the weak force, see Grohs et al. 2018). They affect the interior structure because the pressure is mostly due to free electrons and in some cases (e.g., electron-capture supernovae) weak reactions change the number of free electrons. Neutrino losses modify the energy budget, and dominate for C-burning and beyond. Finally, they affect the nucleosynthesis because the production of most nuclei is sensitive to the electron-to-baryon ratio.

Table 3
Solar Neutrino Fluxes

Component	AGSS09	GS98	Observed[a]
$\Phi_{\rm pp}$	6.01	5.98	$6.05\ (1^{+0.003}_{-0.011})$
$\Phi_{\rm Be}$	4.71	4.95	$4.82\ (1^{+0.05}_{-0.04})$
$\Phi_{\rm B}$	4.62	5.09	$5.00\ (1 \pm 0.03)$
$\Phi_{\rm N}$	2.25	2.91	$\leqslant 6.7$
$\Phi_{\rm O}$	1.67	2.21	$\leqslant 3.2$

Note.
[a] Neutrino observations from the Borexino Collaboration (Bellini et al. 2011) as presented in Haxton et al. (2013) and Villante et al. (2014). The scales for neutrino fluxes Φ (in $\rm cm^{-2}\ s^{-1}$) are: 10^{10} (pp); 10^9 (Be); 10^6 (B); 10^8 (N); and 10^8 (O).

Figure 2 shows the stellar evolution tracks of the models considered in a photon and neutrino H-R diagram. A photon H-R diagram uses two surface properties, the effective temperature $T_{\rm eff}$ and photon luminosity L_γ. A neutrino H-R diagram uses the $T_{\rm eff}$ surface property and an interior property, the neutrino luminosity L_ν. We next discuss the key phases of evolution that are labeled in the neutrino H-R diagram.

Each PMS model begins with a uniform composition and central temperature that is low enough that nuclear burning is inconsequential. The central temperature and density then increase as the stellar model undergoes gravitational contraction. The initial CNO abundances for solar metallicity stars is not equal to the CNO abundances when the CNO cycle is operating in equilibrium. Nuclear reactions replace gravitational contraction as the major source of L_γ and L_ν by burning the ^{12}C abundance to a value that is commensurate with CNO equilibrium values (Iben 1965).

The reactions $^{12}{\rm C}(p,\gamma)^{13}{\rm N}(,e^+\nu_e)^{13}{\rm C}(p,\gamma)^{14}{\rm N}$ can occur at lower temperatures than when the full CNO cycle competes with the pp-chain. They produce a nuclear energy $E_{\rm nuc} \simeq N_{\rm A} Q \rho X_c / {\rm A}_c$, where $N_{\rm A}$ is the Avogadro number, ρ is the mass density, X_c is the mass fraction of ^{12}C, A_c is the number of nucleons in ^{12}C, and $Q \simeq 11$ MeV is the nuclear binding energy release. The thermal energy is $E_{\rm th} \simeq 3/2 N_{\rm A} \rho k_{\rm B} T$, where $k_{\rm B}$ is the Boltzmann constant and T is the temperature. The ratio at solar metallicity and $T = 10^7$ K is $E_{\rm nuc}/E_{\rm th} \simeq Q X_c/(18 k_{\rm B} T) \simeq 1.5$ (Bildsten 2019). That is, the star can delay gravitational contraction for about one Kelvin–Helmholtz timescale by reducing ^{12}C. This transition from the PMS to the zero-age main sequence (ZAMS) is visible in the neutrino H-R diagram of Figure 2 as the loop prior to landing on the ZAMS.

For all of the models considered, core H-burning powers L_ν on the ZAMS by the weak reactions given in Section 2.2. As H in the core depletes, all the models enter the terminal-age main sequence (labeled TAMS in Figure 2) and continue to evolve toward cooler $T_{\rm eff}$. Further evolution is now divided into low-mass stars (Section 3.1) and high-mass stars (Section 3.2).

3.1. Low-mass Stars

Low-mass stars ($M \lesssim 8\ M_\odot$) ascend the red giant branch (labeled RGB in Figure 2) as they evolve to cooler $T_{\rm eff}$ in the photon H-R diagram, and evolve at approximately constant L_ν from shell H-burning in the neutrino H-R diagram.

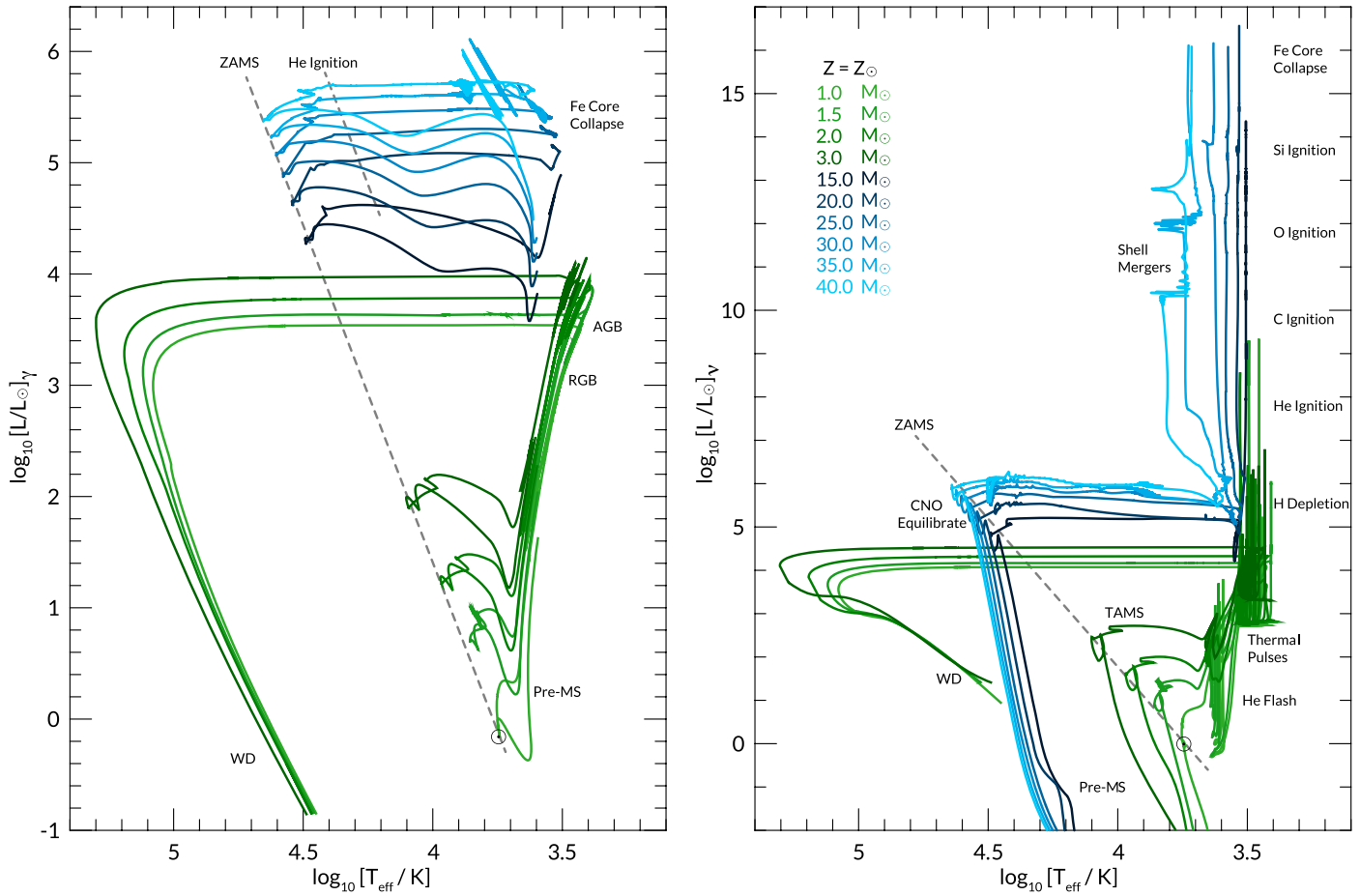

Figure 2. Stellar evolution tracks in a photon H-R diagram (left) and a neutrino H-R diagram (right). Tracks for low-mass stars are shades of green and those for high-mass stars are shades of blue. Luminosities are normalized by their respective current solar values, $L_{\gamma,\odot} = 3.828 \times 10^{33}$ erg s^{-1} (Prša et al. 2016) and $L_{\nu,\odot} = 0.02398 \cdot L_{\gamma,\odot} = 9.1795 \times 10^{31}$ erg s^{-1} (see Section 2.2), and key evolutionary phases are labeled.

As stars evolve, the ashes of nuclear burning usually have a heavier mean atomic number and lie interior to the unburned fuel. For example, the He core is interior to the H-burning shell, and the CO core is interior to the He-burning shell. One class of exceptions occurs when a combination of electron degeneracy and thermal neutrino losses lead to cooler temperatures in the central regions and the fuel ignites off-center. Examples include He ignition in $M_{\rm ZAMS} \lesssim 2M_\odot$ stars (i.e., the "helium flash") and C-ignition in super-asymptotic giant branch (AGB) stars. Fuels that ignite off-center develop convection behind the nuclear burning (toward the surface of the star) and propagate toward the center. These convectively bounded flames have relatively slow speeds (Timmes et al. 1994; García-Berro et al. 1997; Schwab et al. 2020), due to the propagation being driven by thermal conduction under semi-degenerate conditions.

Helium ignition occurs at the tip of the RGB in the photon H-R diagram and in the lower-right in the neutrino H-R diagram. The slowest step in the H-burning CNO cycle is the proton capture onto ^{14}N. This results in all the CNO catalysts piling up into ^{14}N when core H-burning is complete. During He-burning, all of the ^{14}N is converted in ^{22}Ne by the reaction sequence $^{14}{\rm N}(\alpha,\gamma)^{18}{\rm F}(,e^+\nu_e)^{18}{\rm O}(\alpha,\gamma)^{22}{\rm Ne}$. It is the weak reaction in this sequence that powers L_ν throughout this phase of evolution (e.g., Serenelli & Fukugita 2005).

The He core-flash phase, which occurs in $M_{\rm ZAMS} \lesssim 2\,M_\odot$ stars, is characterized by a series of subflashes that propagate toward the stellar center (Thomas 1967; Serenelli & Weiss 2005; Bildsten et al. 2012; Gautschy 2012; Serenelli et al. 2017). For example, the 1 $M_\odot$ model in Figure 2 undergoes five subflashes with the first subflash occurring at $\simeq 0.18\,M_\odot$ and reaching $L_\nu \simeq 10^4\,L_{\nu,\odot}$. The number of subflashes decreases as the stellar mass increases, and the initial flash takes place closer to the stellar center. These subflashes, with their dependence on the stellar mass, are visible in the neutrino H-R diagram of Figure 2 as the spikes in the region labeled "He Flash." After the He core-flash phase, which burns very little helium, core He-burning then proceeds quiescently (e.g., deBoer et al. 2017) to produce an electron degenerate CO core.

Helium ignition in $M_{\rm ZAMS} \gtrsim 2M_\odot$ stars occurs under non-degenerate conditions, without flashes or subflashes, and leads to a different, smoother, signature in the production of neutrinos from ^{18}F decay. For the $2\,M_\odot$ model, from Figure 2, $L_\nu = 0.8\,L_{\gamma,\odot}$ and $L_\gamma = 16\,L_{\gamma,\odot}$ on the MS, $L_\nu = 120\,L_{\gamma,\odot}$ and $L_\gamma = 1750\,L_{\gamma,\odot}$ at He ignition (tip of the RGB), $L_\nu = 5.1\,L_{\gamma,\odot}$ and $L_\gamma = 110\,L_{\gamma,\odot}$ at core He depletion (mass fraction of ^{4}He less than 0.001), $L_\nu = 420\,L_{\gamma,\odot}$ and $L_\gamma = 6100\,L_{\gamma,\odot}$ after the thermal pulses when the envelope mass is $0.01\,M_\odot$, $L_\nu = 1.8\,L_{\gamma,\odot}$ when $L_\gamma = 1.0\,L_{\gamma,\odot}$ on the WD cooling track.

AGB stars are the final stage of evolution driven by nuclear burning. This phase is characterized by H and He burning in geometrically thin shells on top of the CO core (Herwig 2005). For the more massive super-AGB stars a ONeMg core is produced from a convectively bounded carbon flame that propagates toward the center (Becker & Iben 1979, 1980;

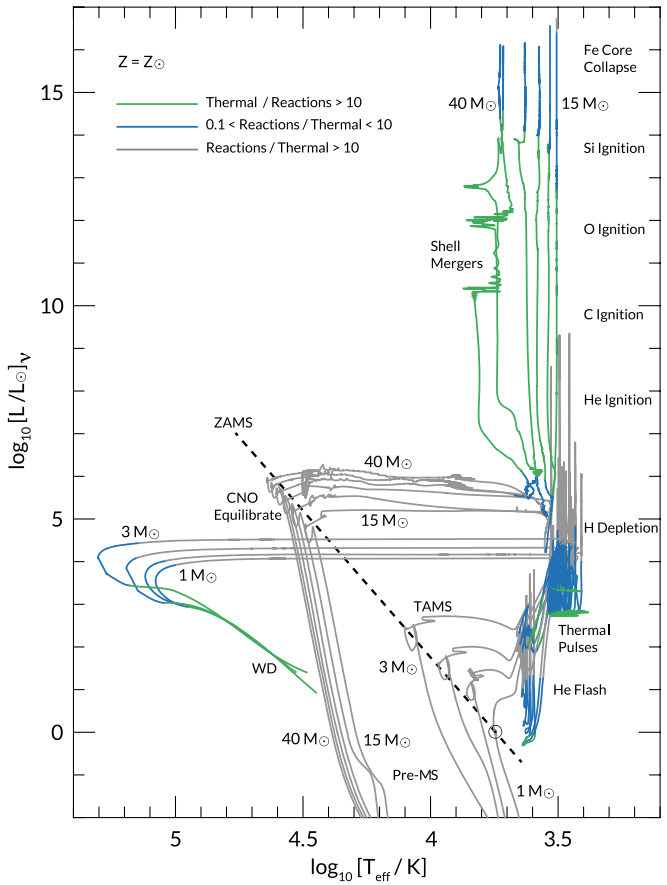

Figure 3. Ratio of the nuclear reaction neutrino luminosity to the thermal neutrino luminosity plotted along stellar evolution tracks in a neutrino H-R diagram. Gray curves indicate where nuclear reaction neutrinos dominate, green curves where thermal neutrinos dominate, and blue curves where the reaction and thermal neutrino luminosities are within a factor of 10. The neutrino luminosity is normalized by the current solar value $L_{\nu,\odot} = 0.02398 \cdot L_{\gamma,\odot} = 9.1795 \times 10^{31}$ erg s^{-1} (see Section 2.2).

García-Berro et al. 1997; Siess 2007; Denissenkov et al. 2015; Farmer et al. 2015; Lecoanet et al. 2016).

A thin He shell grows as material from the adjacent H-burning shell is processed, causing the He shell to increase in temperature and pressure. Once the mass in the He shell reaches a critical value, He ignition causes a thermal pulse. For example, the 3 $M_\odot$ model goes through a series of six thermal pulses, with an interpulse period of $\simeq 10^5$ yr. The number of thermal pulses a model undergoes is poorly determined as the number is sensitive to the mass resolution, the stellar mass-loss rate, and the treatment of convective boundaries. These thermal pulses are visible in the neutrino H-R diagram of Figure 2 as the spikes in the region labeled "thermal pulses."

The stellar models leave the thermal pulse phase when the envelope mass above the still active H and He burning shells is reduced to $\simeq 0.01$ $M_\odot$ by stellar winds. All the low-mass models then evolve toward larger $T_{\rm eff}$ at nearly constant L_ν and L_γ. Nuclear burning extinguishes as the post-AGB model enters the WD cooling track. Plasmon neutrino emission then dominates the energy loss budget for average-mass CO WDs with $T_{\rm eff} \gtrsim 25{,}000$ K (Vila 1966; Kutter & Savedoff 1969; Bischoff-Kim & Montgomery 2018). As the WD continues to cool, photons leaving the surface begin to dominate the cooling as the electrons transition to a strongly degenerate plasma (van Horn 1971; Córsico et al. 2019). The low-mass models in Figure 2 are arbitrarily chosen to terminate when the WD reaches $L_\gamma = 0.1\ L_{\gamma,\odot}$. With $T_{\rm eff} \simeq 30{,}000$ K at this arbitrary termination point, the WD models are still dominated by thermal neutrino cooling, $L_\nu/L_\gamma \simeq 3$ (Winget et al. 2004). For calculating the integrated neutrino background from stellar sources, especially if WDs are abundant, these models should be further evolved to $T_{\rm eff} \lesssim 12{,}000$ K to drive $L_\nu/L_\gamma \leqslant 10^{-5}$ (e.g., Figure 5 in Timmes et al. 2018).

3.2. High-mass Stars

High-mass stars ($M \gtrsim 8\ M_\odot$) in Figure 2 evolve at nearly constant L_ν and L_γ as hydrogen depletes in the core and the models evolve to cooler $T_{\rm eff}$. Free streaming neutrinos from thermal processes, primarily pair annihilation, dominate a star's energy loss budget from the core C-burning phase to core Si depletion. For the 30 $M_\odot$ model, from Figure 2, $L_\nu = 8.2 \times 10^3\ L_{\gamma,\odot}$ and $L_\gamma = 1.2 \times 10^5\ L_{\gamma,\odot}$ on the MS, $L_\nu = 1.3 \times 10^4\ L_{\gamma,\odot}$ and $L_\gamma = 3.0 \times 10^5\ L_{\gamma,\odot}$ at core He ignition, $L_\nu = 5.3 \times 10^3\ L_{\gamma,\odot}$ and $L_\gamma = 2.7 \times 10^5\ L_{\gamma,\odot}$ at core He-depletion (mass fraction of ^{4}He less than 0.001), $L_\nu = 3.2 \times 10^7\ L_{\gamma,\odot}$ and $L_\gamma = 3.1 \times 10^5\ L_{\gamma,\odot}$ at core C-ignition. This dominance over photons as the primary energy loss mechanism sets a rapid evolutionary timescale (years to hours) for the advanced stages of nuclear fusion in pre-supernova stars (Woosley et al. 2002). This rapid evolution is visible in the neutrino H-R diagram of Figure 2 as the nearly vertical curves at approximately constant $T_{\rm eff}$.

Weak reactions that increase the electron-to-baryon ratio during C-burning include β-processes involving ^{23}Mg and ^{21,22}Na. The composition continues to become more neutron-rich during O-burning from β-processes on ^{30,33}P, ^{33}P, ^{35}Cl, and ^{37}Ar Core Si-burning is the last exothermic burning stage and produces the Fe-peak nuclei. Many isotopes in this stage of evolution undergo β-processes that continue to make the material more neutron-rich (see Heger et al. 2001; Odrzywolek 2009; Patton et al. 2017b).

Dynamical large-scale mixing on nuclear burning timescales occurs during the late stages of evolution in massive stars. Stellar evolution models suggest that merging occurs between the C, Ne, O, and Si shells. These shell mergers are beginning to be explored with 3D hydrodynamic simulations (e.g., Ritter et al. 2018). The approximate location of these shell mergers is labeled in the neutrino H-R diagram. In addition, the energetics of nuclear burning tightly couples to turbulent convection during O-burning and Si-burning. This strong coupling must be modeled with 3D simulations (Meakin & Arnett 2007; Couch et al. 2015; Müller et al. 2017; Fields & Couch 2020) to assess the fidelity of the convection approximations made by 1D models.

When the Fe core reaches its finite-temperature Chandrasekhar mass, electron capture and photodisintegration drive collapse of the Fe core, with the largest infall speeds usually occurring near the outer edge of the Fe core. The massive star models in Figure 2 terminate when any mass coordinate within the Fe core exceeds an inward velocity of 300 km s^{-1}.

3.3. Reaction and Thermal Neutrino Luminosities

Figure 3 shows the ratio of nuclear reaction neutrinos to thermal neutrinos along the stellar evolution tracks in the neutrino H-R diagram. Broadly, neutrinos from reactions dominate during H and He burning, and thermal neutrinos

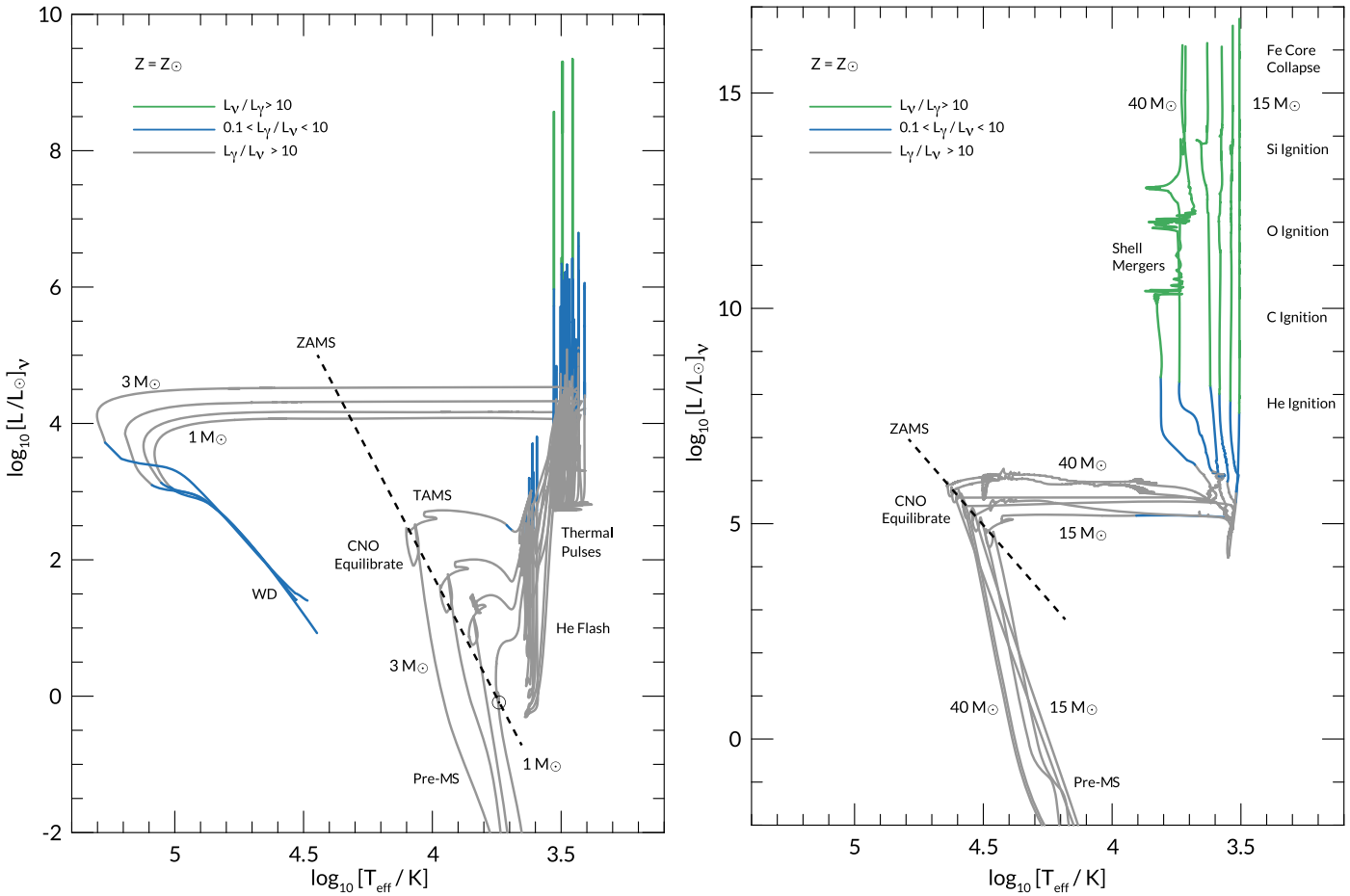

Figure 4. Ratio of the photon luminosity to the neutrino luminosity in a neutrino H-R diagram. Low-mass stars are on the left, high-mass stars on the right. Gray curves indicate where photons dominate, green curves where neutrinos dominate, and blue curves where the photon and neutrino luminosities are within a factor of 10. The neutrino luminosity is normalized by the current solar value $L_{\nu,\odot} = 0.02398 \cdot L_{\gamma,\odot} = 9.1795 \times 10^{31}$ erg s^{-1} (see Section 2.2).

dominate for C-burning onwards. There are exceptions to this general scenario. One exception is between the subflashes of the He flash for low-mass stars, where thermal neutrinos become comparable or larger than neutrino losses from reactions. Another exception is between thermal pulses on the AGB where thermal neutrinos are again comparable or larger than nuclear reaction neutrinos. Conversely, nuclear reaction neutrinos are comparable to, but less than, thermal neutrinos during the final phases of massive star evolution.

3.4. Photon and Neutrino Luminosities

Figure 4 shows the L_γ/L_ν ratio along the stellar evolution tracks in the neutrino H-R diagram. Photons dominate over most of a star's lifetime (e.g., Barkat 1975), except in the advanced stages of evolution, where neutrinos dominate on the early portions of the WD cooling tracks for low-mass stars and for carbon burning to the onset of core collapse for high-mass stars.

4. Discussion and Summary

Using a MESA solar-calibrated model for the Sun's neutrino luminosity as a normalization (Section 2.2), we have explored the evolution of a select grid of stellar models from their PMS phase to near their final fates in a neutrino H-R diagram (Figure 2). We also delineated the contributions from reaction and thermal neutrinos during a model's evolution (Figure 3). This is the first time, to our knowledge, that such an exploration with a different messenger, neutrinos, has been presented in the literature.

Neutrino astronomy is a unique tool that can yield insights into otherwise hidden aspects of stellar astrophysics (Bahcall 1989; Beacom 2010). However, the small cross section between neutrinos and baryonic matter, which allows neutrinos to escape from the star in the first place, means it is unlikely that near-future neutrino detectors will be able to probe the neutrino luminosity tracks shown in Figure 2.

A possible exception is the evolution of a pre-supernova star on timescales of a $\simeq$10 hr before Fe core collapse. For a normal neutrino mass hierarchy, more than 200 events could be detected before core collapse for a 15–30 $M_\odot$ star at $\simeq$200 pc (e.g., α Orionis, Betelgeuse), and neutrino emission may be detectable within $\simeq$600 pc with the improved sensitivity of Super-Kamiokande with Gadolinium (Patton et al. 2017b; Simpson et al. 2019).

Another possible exception is the detection of neutrinos from the He flash and thermal pulses of low-mass stars. Figures 2 and 3 suggest the He flash reaches peaks of $L_\nu \simeq 10^4\ L_{\nu,\odot}$ and is driven by the ^{18}F(,$e^+\nu_e$)^{18}O reaction (Serenelli & Fukugita 2005). The maximum energy of neutrinos emitted by this reaction is $\simeq$0.6 MeV and the average energy is $\simeq$0.3 MeV. The neutrino flux is thus $\Phi_{\nu,\text{He flash}} \simeq 170\ (10\ \text{pc}/d)^2\ \text{cm}^{-2}\ \text{s}^{-1}$ for a star located at a distance of d parsec. The timescale of this peak emission is $\simeq$3 days, depending chiefly on the initial ZAMS mass. Figures 2 and 3 also suggest that the He-burning

driven thermal pulses reach peaks of $L_\nu \simeq 10^9\ L_{\nu,\odot}$ from the same $^{18}\mathrm{F}(,e^+\nu_e)^{18}\mathrm{O}$ reaction with an average energy of $\simeq$0.3 MeV. This gives a neutrino flux of $\Phi_{\nu,\mathrm{TP}} \simeq 1.7 \times 10^7$ $(10\ \mathrm{pc}/d)^2\ \mathrm{cm}^{-2}\ \mathrm{s}^{-1}$ on timescales of $\simeq$0.1 yr, depending on the mass of the stellar envelope, uncertain mass-loss rate, and pulse number. Finally, integration of the neutrino luminosity stellar evolution tracks may be useful for refining estimates of the diffuse stellar neutrino background (Horiuchi et al. 2009; Beacom 2010).

We thank the anonymous referee for improving this article, and Aaron Dotter, Thomas Steindl, and Josiah Schwab for discussions. The MESA project is supported by the National Science Foundation (NSF) under the Software Infrastructure for Sustained Innovation program grants (ACI-1663684, ACI-1663688, ACI-1663696). This research was also supported by the NSF under grant PHY-1430152 for the Physics Frontier Center "Joint Institute for Nuclear Astrophysics—Center for the Evolution of the Elements" (JINA-CEE). R.F. is supported by the Netherlands Organization for Scientific Research (NWO) through a top module 2 grant with project number 614.001.501 (PI de Mink). F.X.T. acknowledges stimulating discussions at Sky House. This research made extensive use of the SAO/NASA Astrophysics Data System (ADS).

Software: MESA (Paxton et al. 2011, 2013, 2015, 2018, 2019; http://mesa.sourceforge.net), MESASDK 20190830 (Townsend 2019a, 2019b), matplotlib (Hunter 2007), and NumPy (van der Walt et al. 2011).

ORCID iDs

Ebraheem Farag https://orcid.org/0000-0002-5794-4286
F. X. Timmes https://orcid.org/0000-0002-0474-159X
Morgan Taylor https://orcid.org/0000-0002-5107-8639
Kelly M. Patton https://orcid.org/0000-0002-2154-4782
R. Farmer https://orcid.org/0000-0003-3441-7624

References

Alastuey, A., & Jancovici, B. 1978, ApJ, 226, 1034
Albert, A., André, M., Anghinolfi, M., et al. 2017, ApJL, 850, L35
Alekseev, E. N., Alekseeva, L. N., Volchenko, V. I., & Krivosheina, I. V. 1987, JETPL, 45, 589
Althaus, L. G., Córsico, A. H., Isern, J., & García-Berro, E. 2010, A&AR, 18, 471
Angulo, C., Arnould, M., Rayet, M., et al. 1999, NuPhA, 656, 3
Asplund, M., Grevesse, N., Sauval, A. J., & Scott, P. 2009, ARA&A, 47, 481
Aufderheide, M. B. 1993, ApJ, 411, 813
Badnell, N. R., Bautista, M. A., Butler, K., et al. 2005, MNRAS, 360, 458
Bahcall, J. N. 1989, Neutrino Astrophysics (Cambridge: Cambridge Univ. Press)
Bahcall, J. N., & Pinsonneault, M. H. 1992, RvMP, 64, 885
Bahcall, J. N., Serenelli, A. M., & Basu, S. 2005, ApJL, 621, L85
Bahcall, J. N., & Ulmer, A. 1996, PhRvD, 53, 4202
Barkat, Z. 1975, ARA&A, 13, 45
Basu, S., & Antia, H. M. 1997, MNRAS, 287, 189
Basu, S., & Antia, H. M. 2004, ApJL, 606, L85
Basu, S., Chaplin, W. J., Elsworth, Y., New, R., & Serenelli, A. M. 2009, ApJ, 699, 1403
Beacom, J. F. 2010, ARNPS, 60, 439
Beaudet, G., Petrosian, V., & Salpeter, E. E. 1967, ApJ, 150, 979
Becker, S. A., & Iben, I., Jr. 1979, ApJ, 232, 831
Becker, S. A., & Iben, I., Jr. 1980, ApJ, 237, 111
Bellini, G., Benziger, J., Bick, D., et al. 2011, PhRvL, 107, 141302
Bergemann, M., & Serenelli, A. 2014, in Solar Abundance Problem, ed. E. Niemczura, B. Smalley, & W. Pych (Cham: Springer), 245
Bildsten, L. 2019, MESA Summer School: Approaching the Main Sequence, v1 Zenodo, doi:10.5281/zenodo.3374948
Bildsten, L., Paxton, B., Moore, K., & Macias, P. J. 2012, ApJL, 744, L6
Bionta, R. M., Blewitt, G., Bratton, C. B., et al. 1987, PhRvL, 58, 1494
Birkl, R., Aloy, M. A., Janka, H. T., & Müller, E. 2007, A&A, 463, 51
Bischoff-Kim, A., & Montgomery, M. H. 2018, AJ, 155, 187
Borexino Collaboration, Agostini, M., Altenmüller, K., et al. 2018, Natur, 562, 505
Bouvier, A., & Wadhwa, M. 2010, NatGe, 3, 637
Brugière, T. 2017, NIMPA, 845, 326
Catelan, M., de Freitas Pacheco, J. A., & Horvath, J. E. 1996, ApJ, 461, 231
Choi, J., Dotter, A., Conroy, C., et al. 2016, ApJ, 823, 102
Christensen-Dalsgaard, J., Monteiro, M. J. P. F. G., Rempel, M., & Thompson, M. J. 2011, MNRAS, 414, 1158
Chugunov, A. I., Dewitt, H. E., & Yakovlev, D. G. 2007, PhRvD, 76, 025028
Córsico, A. H., Althaus, L. G., Miller Bertolami, M. M., & Kepler, S. O. 2019, A&ARv, 27, 7
Couch, S. M., Chatzopoulos, E., Arnett, W. D., & Timmes, F. X. 2015, ApJL, 808, L21
Cristini, A., Hirschi, R., Meakin, C., et al. 2019, MNRAS, 484, 4645
Cristini, A., Meakin, C., Hirschi, R., et al. 2017, MNRAS, 471, 279
Cyburt, R. H., Amthor, A. M., Ferguson, R., et al. 2010, ApJS, 189, 240
deBoer, R. J., Görres, J., Wiescher, M., et al. 2017, RvMP, 89, 035007
Denissenkov, P. A., Truran, J. W., Herwig, F., et al. 2015, MNRAS, 447, 2696
Dewitt, H. E., Graboske, H. C., & Cooper, M. S. 1973, ApJ, 181, 439
Dutta, S. I., Ratković, S., & Prakash, M. 2004, PhRvD, 69, 023005
Farmer, R., Fields, C. E., & Timmes, F. X. 2015, ApJ, 807, 184
Fields, C. E., & Couch, S. 2020, ApJ, submitted
Fontaine, G., Brassard, P., & Bergeron, P. 2001, PASP, 113, 409
Fowler, W. A., & Hoyle, F. 1964, ApJS, 9, 201
Fröhlich, C., Martínez-Pinedo, G., Liebendörfer, M., et al. 2006, PhRvL, 96, 142502
Fryer, C. L., Rueda, J. A., & Ruffini, R. 2014, ApJL, 793, L36
Fujimoto, M. Y., Sztajno, M., Lewin, W. H. G., & van Paradijs, J. 1987, ApJ, 319, 902
Fuller, G. M., Fowler, W. A., & Newman, M. J. 1980, ApJS, 42, 447
Fuller, G. M., Fowler, W. A., & Newman, M. J. 1982a, ApJS, 48, 279
Fuller, G. M., Fowler, W. A., & Newman, M. J. 1982b, ApJ, 252, 715
Fuller, G. M., Fowler, W. A., & Newman, M. J. 1985, ApJ, 293, 1
García-Berro, E., Ritossa, C., & Iben, I., Jr. 1997, ApJ, 485, 765
Gautschy, A. 2012, arXiv:1208.3870
Goodwin, A. J., Heger, A., & Galloway, D. K. 2019, ApJ, 870, 64
Graboske, H. C., Dewitt, H. E., Grossman, A. S., & Cooper, M. S. 1973, ApJ, 181, 457
Grevesse, N., & Sauval, A. J. 1998, SSRv, 85, 161
Grohs, E., Howe, A. R., & Adams, F. C. 2018, PhRvD, 97, 043003
Haxton, W. C., Hamish Robertson, R. G., & Serenelli, A. M. 2013, ARA&A, 51, 21
Heger, A., Woosley, S. E., Martínez-Pinedo, G., & Langanke, K. 2001, ApJ, 560, 307
Herwig, F. 2000, A&A, 360, 952
Herwig, F. 2005, ARA&A, 43, 435
Hirata, K., Kajita, T., Koshiba, M., Nakahata, M., & Oyama, Y. 1987, PhRvL, 58, 1490
Hirata, K. S., Kajita, T., Koshiba, M., et al. 1988, PhRvD, 38, 448
Horiuchi, S., Beacom, J. F., & Dwek, E. 2009, PhRvD, 79, 083013
Hunter, J. D. 2007, CSE, 9, 90
Iben, I. J. 1965, ApJ, 141, 993
IceCube Collaboration, Aartsen, M. G., Ackermann, M., et al. 2018a, Sci, 361, eaat1378
IceCube Collaboration, Aartsen, M. G., Ackermann, M., et al. 2018b, Sci, 361, 147
Iglesias, C. A., & Rogers, F. J. 1996, ApJ, 464, 943
Itoh, N., Adachi, T., Nakagawa, M., Kohyama, Y., & Munakata, H. 1989, ApJ, 339, 354
Itoh, N., Hayashi, H., Nishikawa, A., & Kohyama, Y. 1996a, ApJS, 102, 411
Itoh, N., Mutoh, H., Hikita, A., & Kohyama, Y. 1992, ApJ, 395, 622
Itoh, N., Nishikawa, A., & Kohyama, Y. 1996b, ApJ, 470, 1015
Itoh, N., Totsuji, H., Ichimaru, S., & Dewitt, H. E. 1979, ApJ, 234, 1079
Janka, H.-T. 2017, in Handbook of Supernovae, ed. A. Alsabti & P. Murdin (Cham: Springer), 1575
Jones, S., Hirschi, R., Nomoto, K., et al. 2013, ApJ, 772, 150
Kajino, T., Aoki, W., Balantekin, A. B., et al. 2019, PrPNP, 107, 109
Kato, C., Delfan Azari, M., Yamada, S., et al. 2015, ApJ, 808, 168
Kawaler, S. D., Winget, D. E., Iben, I. J., & Hansen, C. J. 1986, ApJ, 302, 530
Kutschera, M., Odrzywołek, A., & Misiaszek, M. 2009, AcPPB, 40, 3063
Kutter, G. S., & Savedoff, M. P. 1969, ApJ, 156, 1021
Kyutoku, K., & Kashiyama, K. 2018, PhRvD, 97, 103001

Langanke, K., & Martínez-Pinedo, G. 2000, NuPhA, 673, 481
Langanke, K., & Martínez-Pinedo, G. 2014, NuPhA, 928, 305
Lecoanet, D., Schwab, J., Quataert, E., et al. 2016, ApJ, 832, 71
Li, Y.-F. 2014, IJMPS, 31, 1460300
McLaughlin, G. C., & Fuller, G. M. 1995, ApJ, 455, 202
Meakin, C. A., & Arnett, D. 2007, ApJ, 667, 448
Misch, G. W., Sun, Y., & Fuller, G. M. 2018, ApJ, 852, 43
Misiaszek, M., Odrzywołek, A., & Kutschera, M. 2006, PhRvD, 74, 043006
Müller, B., Melson, T., Heger, A., & Janka, H.-T. 2017, MNRAS, 472, 491
Newstead, J. L., Strigari, L. E., & Lang, R. F. 2019, PhRvD, 99, 043006
Nomoto, K., & Tsuruta, S. 1981, ApJL, 250, L19
Oda, T., Hino, M., Muto, K., Takahara, M., & Sato, K. 1994, ADNDT, 56, 231
Odrzywołek, A. 2007, EPJC, 52, 425
Odrzywolek, A. 2009, PhRvC, 80, 045801
Patton, K. M., Lunardini, C., & Farmer, R. J. 2017a, ApJ, 840, 2
Patton, K. M., Lunardini, C., Farmer, R. J., & Timmes, F. X. 2017b, ApJ, 851, 6
Paxton, B., Bildsten, L., Dotter, A., et al. 2011, ApJS, 192, 3
Paxton, B., Cantiello, M., Arras, P., et al. 2013, ApJS, 208, 4
Paxton, B., Marchant, P., Schwab, J., et al. 2015, ApJS, 220, 15
Paxton, B., Schwab, J., Bauer, E. B., et al. 2018, ApJS, 234, 34
Paxton, B., Smolec, R., Schwab, J., et al. 2019, ApJS, 243, 10
Potekhin, A. Y., Pons, J. A., & Page, D. 2015, SSRv, 191, 239
Prša, A., Harmanec, P., Torres, G., et al. 2016, AJ, 152, 41
Raffelt, G., & Weiss, A. 1992, A&A, 264, 536
Ramadurai, S. 1976, MNRAS, 176, 9
Ramadurai, S. 1984, MNRAS, 206, 849
Ratković, S., Iyer Dutta, S., & Prakash, M. 2003, PhRvD, 67, 123002
Ray, A., Chitre, S. M., & Kar, K. 1984, ApJ, 285, 766
Ritter, C., Andrassy, R., Côté, B., et al. 2018, MNRAS, 474, L1
Schinder, P. J., Schramm, D. N., Wiita, P. J., Margolis, S. H., & Tubbs, D. L. 1987, ApJ, 313, 531
Schwab, J., Farmer, R., & Timmes, F. X. 2020, ApJ, 891, 5
Serenelli, A. 2016, EPJA, 52, 78
Serenelli, A., & Weiss, A. 2005, A&A, 442, 1041
Serenelli, A., Weiss, A., Cassisi, S., Salaris, M., & Pietrinferni, A. 2017, A&A, 606, A33
Serenelli, A. M., & Fukugita, M. 2005, ApJL, 632, L33
Siess, L. 2007, A&A, 476, 893
Simpson, C., Abe, K., Bronner, C., et al. 2019, ApJ, 885, 133
Stonehill, L. C., Formaggio, J. A., & Robertson, R. G. 2004, PhRvC, 69, 015801
Sweigart, A. V., & Gross, P. G. 1978, ApJS, 36, 405
Thomas, H.-C. 1967, ZA, 67, 420
Thoul, A. A., Bahcall, J. N., & Loeb, A. 1994, ApJ, 421, 828
Timmes, F. X., Townsend, R. H. D., Bauer, E. B., et al. 2018, ApJL, 867, L30
Timmes, F. X., Woosley, S. E., & Taam, R. E. 1994, ApJ, 420, 348
Townsend, R. 2019a, MESA SDK for Linux, v1, Zenodo, doi:10.5281/zenodo.2669541
Townsend, R. 2019b, MESA SDK for Mac OS, v1, Zenodo, doi:10.5281/zenodo.2669543
Uribe Suárez, J. D., & Rueda Hernandez, J. A. 2019, arXiv:1909.01841
van der Walt, S., Colbert, S. C., & Varoquaux, G. 2011, CSE, 13, 22
van Horn, H. M. 1971, in IAU Symp. 42, White Dwarfs, ed. W. J. Luyten (Dordrecht: Springer), 97
Vila, S. C. 1966, ApJ, 146, 437
Villante, F. L., Serenelli, A. M., Delahaye, F., & Pinsonneault, M. H. 2014, ApJ, 787, 13
Vinyoles, N., Serenelli, A. M., Villante, F. L., et al. 2017, ApJ, 835, 202
Winget, D. E., Sullivan, D. J., Metcalfe, T. S., Kawaler, S. D., & Montgomery, M. H. 2004, ApJL, 602, L109
Woosley, S. E., Hartmann, D. H., Hoffman, R. D., & Haxton, W. C. 1990, ApJ, 356, 272
Woosley, S. E., Heger, A., & Weaver, T. A. 2002, RvMP, 74, 1015
Zhang, Q.-S., Li, Y., & Christensen-Dalsgaard, J. 2019, ApJ, 881, 103